City Research Online

City, University of London Institutional Repository

This is the accepted version of the paper.

This version of the publication may differ from the final published version.

Ink-Jet Printed Graphene Electronics

F. Torrisi, T. Hasan, W. Wu, Z. Sun, A. Lombardo, T. Kulmala, G. W. Hshieh, S. J. Jung, F. Bonaccorso, P. J. Paul, D. P. Chu, A. C. Ferrari

Department of Engineering, University of Cambridge, Cambridge CB3 0FA, U.K

Abstract

We demonstrate ink-jet printing as a viable method for large area fabrication of graphene devices. We produce a graphene-based ink by liquid phase exfoliation of graphite in N-Methylpyrrolidone. We use it to print thin-film transistors, with mobilities up to $\sim 95 \mathrm{cm}^2 \mathrm{V}^{-1} \mathrm{s}^{-1}$, as well as transparent and conductive patterns, with $\sim 80\%$ transmittance and $\sim 30 \mathrm{k\Omega/\square}$ sheet resistance. This paves the way to all-printed, flexible and transparent graphene devices on arbitrary substrates.

Introduction

Flexible electronics is a rapidly expanding research area.[1] Applications include touch screens,[2] electronic paper (e-paper),[3,4] sensors,[5] radio frequency tags,[6] photovoltaic cells,[7,8] and electronic textiles.[9] To date, it mainly relies on two fabrication strategies: one in which substrates bearing thousands of Field-effect Transistors (FETs) are bonded to plastic by transfer printing or pick-and place methods;[10] another in which FETs are prepared directly on the target substrate by several coating, curing and lithographic steps.[1,11] Rubber stamping,[12] embossing[13] and ink-jet printing[14,15] reduce the number of such fabrication steps.

---

*To whom correspondence should be addressed

1

Ink-jet printing is one of the most promising techniques for large area fabrication of flexible plastic electronics.[15] A range of components can be printed, such as transistors,[13,15–18] photovoltaic devices,[19] organic light emitting diodes (OLEDs),[13,18,20] and displays.[13] Ink-jet printing is versatile,[18] involves a limited number of process steps,[21] is amenable for mass production, and can deposit controlled amounts of material.[21] Drop on demand[21,22] ink-jet printing has progressed from printing text and graphics,[21] to a tool for rapid manufacturing,[23] being now a well established technique to print Thin Film Transistor (TFT) based on organic conducting and semiconducting inks.[5,15,24] However, their mobilities, $\mu < 0.5 \text{cm}^2\text{V}^{-1}\text{s}^{-1}$,[5,18] are still much lower than standard silicon technology. Several approaches aim to improve these results, such as the use of polysilicon,[25] zinc oxide nanoparticles[26] and carbon nanotubes (CNTs).[27–32] Metal nanoparticle inks are not stable in ordinary solvents, such as Deionized (DI) Water, Acetone, Isopropyl Alcohol, N-Methylpyrrolidone (NMP), Tetrahydrofuran.[18,33] Therefore they need to be chemically modified in order to be dispersed,[18] via the use of stabilizers, which usually degrade in a couple of years.[18,33] Metal nanoparticles also tend to oxidize after the printing process.[18,33] Ink-jet printed CNT-TFTs have been reported with μ up to $50\text{cm}^2 \text{V}^{-1}\text{s}^{-1}$ and a ON/OFF ratio~10^3.[32]

Graphene is the two-dimensional (2d) building block for sp^2 carbon allotropes of every other dimensionality. It can be stacked into 3d graphite, rolled into 1d nanotubes, or wrapped into 0d fullerenes.[34] It is at the centre of an ever expanding research area.[34–37] Near-ballistic transport and high mobility make it an ideal material for nanoelectronics, especially for high frequency applications.[38] Furthermore, its optical and mechanical properties are ideal for micro and nanomechanical systems, thin-film transistors, transparent and conductive composites and electrodes, and photonics.[34,37,39] Graphene was isolated by micromechanical exfoliation of graphite.[40] This technique still gives the best samples in terms of purity, defects, mobility and optoelectronics properties. However, large scale production approaches are needed for widespread application. These encompass growth by chemical vapor deposition (CVD),[41–46] segregation by heat treatment of silicon carbide[47–50] and metal substrates,[51–54] liquid phase exfoliation (LPE).[55–58] Amongst these, LPE is ideally suited to produce printable inks.

Graphite can be exfoliated by chemical wet dispersion followed by ultrasonication, both in aqueous[56,58] and non-aqueous solvents.[55,58] Dispersions can be achieved by mild sonication of graphite in water with Sodium Deoxycholate followed by sedimentation based-ultracentrifugation.[58,59] Bile salt surfactants also allow the isolation of flakes with controlled thickness, when combined with density gradient ultracentrifugation (DGU).[60] Exfoliation of graphite intercalated compounds[57] and expandable graphite[61] was also reported.

LPE was first achieved through sonication of graphite oxide,[62] following the Hummers method.[63] The oxidation of graphite in the presence of acids and oxidants[64,65] disrupts the sp^2-network and introduces hydroxyl or epoxide groups,[66,67] with carboxylic or carbonyl groups attached to the edge.[66,67] These make GO sheets readily dispersible in water[62,68] and several other solvents.[69] Although large GO flakes can be produced, these are intrinsically defective,[62,70] and electrically insulating.[62,66] Despite several attempts,[62,66] reduced GO (RGO) does not fully regain the pristine graphene electrical conductivity.[66,71] It is thus important to distinguish between dispersion processed graphene flakes,[55–58] retaining the electronic properties of graphene, and insulating GO dispersions.[62,71] Several groups reported GO-based inks.[33,72,73] Ref.[72] ink-jet printed RGO films for sensors applications, while Ref.[33] produced RGO-stabilized Cu nanoparticles as low temperature metal colloids, to replace standard metal nanoparticle inks, that require high temperature sintering postprocessing.[74] Mobilities up to $90 cm^2 V^{-1} s^{-1}$ have been achieved for highly reduced GO films by ink-jet printing,[73] with an ON/OFF ratio up to 10.[73]

Here we produce a graphene-based ink and demonstrate its viability for printed electronics.

Results and discussion

Ink requirements

A key property of inks viable for printing is their ability to generate droplets.[75,76] Ink viscosity, η [mPa s], surface tension, γ [mJ m^{-2}], density, ρ [g cm^{-3}], and nozzle diameter, a [μm],

influence the spreading of the resulting liquid drops.[75–77] These can be arranged into dimension-less figures of merit (FOM), such as the Reynolds (Re),[75–77] Weber (We),[75–77] and Ohnesorge (Oh)[75–77] numbers: Re=$\frac{\upsilon\rho a}{\eta}$; We=$\frac{\upsilon^2\rho a}{\gamma}$, Oh=$\frac{\sqrt{We}}{Re} = \frac{\eta}{\sqrt{\gamma\rho a}}$, where υ[m/s] is the drop velocity.

Refs.[75–77] suggested to use Z=1/Oh as the appropriate FOM to characterize drop formation, 1<Z<14 being required to get stable drop generation.[75,76] For Z<1 the high viscosity prevents drop ejection,[75,76] whereas at Z>14 the primary drop is accompanied by a number of satellite droplets.[75,76] Moreover, when inks contain dispersed molecules or nano-particles, the latter should be smaller than the nozzle diameter, to prevent clogging.[21,23] Refs.[23,78] suggested that the size of such molecules or particles should be at least 1/50 of the nozzle diameter, in order to exclude any printing instability, such as clustering of the particles at the nozzle edge, which may deviate the drop trajectory, or result in agglomerates that will eventually block the nozzle.

The ejected drop behavior on the substrate can be efficiently described by fluid dynamics. When a small liquid droplet is in contact with a flat surface, partial wetting results in a finite angle between the liquid and the substrate,[79] known as contact angle, θ_C.[79–81] The lower drop size limit is given by[75,76] $s[\mu m] = a\sqrt{\frac{We+12}{3(1-cos\theta_C)+4We/Re^{1/2}}}$. Thus, e.g., for a typical a=50μm, We=20, Re=58 and $\theta_C\sim$45°, we get $s\sim$85-90μm. The distance from the substrate must be optimized to guarantee both homogeneous printing and the highest resolution, barring any unusual jetting conditions, such as perturbations from the surrounding environment and diversion of the drop trajectory.[18,75,82] Furthermore, a substrate very close to the nozzle causes secondary drops to scatter off during the impact of the primary drop,[18,83] due to the initial drop jetting pressure, thus affecting the homogeneity of the final printed features.[83] The final assembly of printed nano-particle inks depends on the substrate Surface Energy (SE),[21,23] as well as the ink viscosity and surface tension.[21]

When a drop of an ink containing dispersed particles evaporates on a surface it commonly leaves a dense, ring-like, deposit along its perimeter.[21,23] This is the so-called "coffee ring effect",[84] i.e. a distortion of the drops during solvent drying due to the interplay of ink viscosity and solute transport via solvent motion (arising from surface tension interaction between solvent and substrate).[18,84] This is one of the most important phenomena affecting the homogeneity of

4

ink-jet printed drops.[18,84] In order to prevent this, it is necessary to "freeze" the drops geometry immediately after they form an homogeneous and continuous film on the substrate.[18]

Here we use an ink-jet printer with a nozzle diameter$\sim 50\mu$m, thus we need to have flakes less than 1μm across. By tuning η, γ and ρ we will target a Z within the optimal range. We print on Si/SiO$_2$ (because we want to probe the electrical properties of our graphene-ink) and borosilicate (Pyrex 7740-Polished Prime Grade) glass substrates (because we want to test graphene-ink as transparent conductor), both with a roughness R$_z$<15nm. Our aim is to obtain ink-jet printed drops, on substrate, with homogeneous flakes and uniform morphology, i.e. with roughness comparable to the substrate. We obtain this by varying the contact angle and optimizing the substrate wettability.

In order to reduce the coffee ring effect we need both a solvent with boiling point (T$_c$ [$^\circ$C]) and heat of vaporization (V$_c$ [kJ/mol]) higher than water,[18,82,84] and a substrate which promotes adhesion.[85] Thus we use NMP as solvent for two main reasons. First, it has higher boiling point ($\sim 202^\circ$C)[86] and heat of vaporization (54.5kJ/mol),[86] than water ($\sim 100^\circ$C and ~ 40kJ/mol). Second, NMP is the best solvent to get high-yield, surfactant-free exfoliation of graphite.[55,58] We then test several surface treatments to optimize substrate adhesion. After printing NMP is removed by a thermal annealing at 170°C for 5 minutes.

Graphene-based printable ink

We prepare the graphene-based printable ink as follows. Graphite flakes (NGS Naturgraphit) are sonicated (Decon bath, 20W) in NMP for 9 hours. The un-exfoliated flakes are left to settle for 10 mins after sonication. The decanted dispersions are then ultracentrifuged using a TH-641 swinging bucket rotor in a Sorvall WX-100 Ultra-centrifuge at 10,000 rpm ($\sim 15,000$g) for an hour and filtered to remove flakes>1μm, that might clog the nozzle. The resulting ink is characterized by Optical Absorption Spectroscopy (OAS), High Resolution Transmission Electron Microscopy (HRTEM), Electron diffraction and Raman spectroscopy (see Methods).

OAS can be used to estimate the concentration of graphene[55,56,59] using the Beer-Lambert Law according to the relation $A = \alpha c l$, where A is the absorbance, l [m] is the light path length, c [g/L]
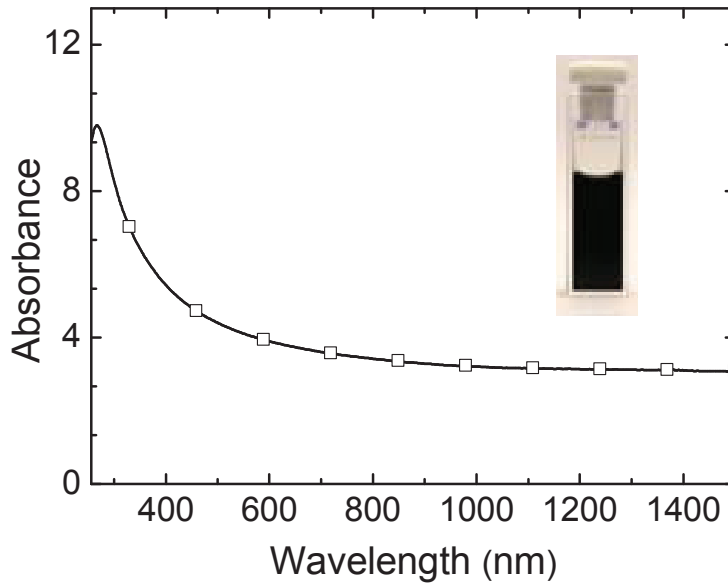
Figure 1: Absorbance of our graphene-ink. The inset is a picture of a vial of ink.

the concentration of dispersed graphitic material and α [L g^{-1} m^{-1}] the absorption coefficient. Figure 1 plots an OAS spectrum of our ink diluted to 10%. The ink is diluted to avoid strong scattering losses at higher concentrations, which could cause deviation of the measured value of A from the Beer-Lambert law. The spectrum in Figure 1 is mostly featureless, as expected due to linear dispersion of the Dirac electrons,[37,39,87–90] the peak in the UV region being a signature of the van Hove singularity in the graphene density of states.[88] From $\alpha \sim 1390$Lg^{-1}m^{-1} at 660nm, as for Refs.,[56,58] we estimate c$\sim$0.11$\pm$0.02g/L.

Figure 2a is HRTEM image of a Single Layer Graphene (SLG) flake from the ink, while Figure 2b is a normal-incidence electron diffraction of the same flake of Figure 2a. It shows the expected sixfold symmetry.[91–93] The peaks are labeled with the corresponding Miller-Bravais (hkil) indexes. For Few Layer Gaphene (FLG) flakes with Bernal (AB) stacking, the intensity ratio I_{1100}/I_{2110} is<1, while for SLG I_{1010}/I_{2110}>1.[91,93] We use this to distinguish SLG from FLGs.[55,59] Figure 2c plots the diffraction intensity measured along the line section through the $(1\bar{2}10)$, $(0\bar{1}10)$, $(\bar{1}010)$, $(\bar{2}110)$ axis, reported in Figure 2b. The inner peaks, $(0\bar{1}10)$ and $(\bar{1}010)$, are$\sim$1.5 times more intense than the outer ones, $(1\bar{2}10)$ and $(\bar{2}110)$, indicating that the flake is SLG.[91] The analysis of the edges also gives a reliable information on the number of layers and can be used to investigate a
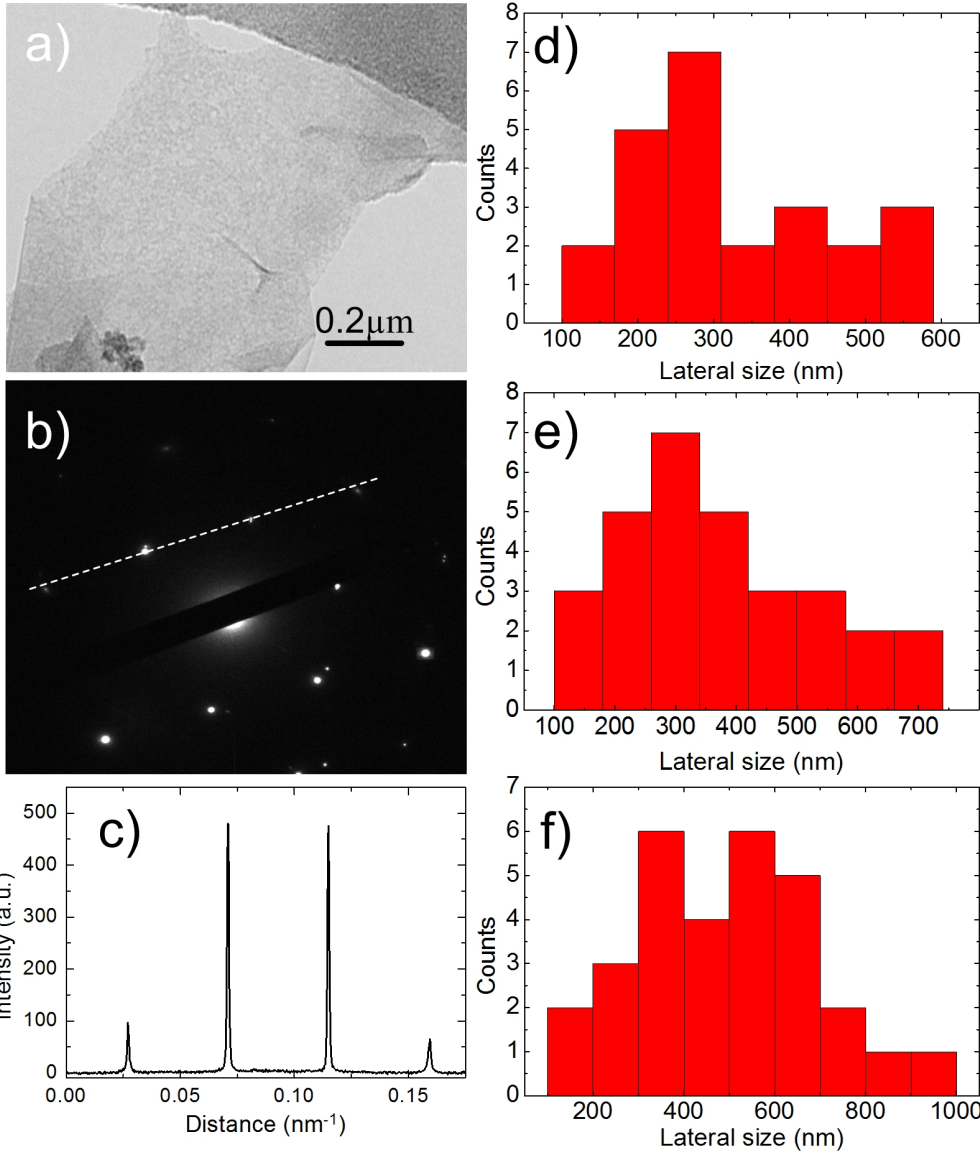
6

Figure 2: a,b) HRTEM image and electron diffraction pattern of dispersion-cast SLG. c) Diffracted intensity along the dashed line in b. Statistics of lateral size for d) SLGs, e) BLGs and f) FLGs.

large number of flakes,[91] from zoomed-in high resolution edge images.[55,94] If SLG folds or several SLGs stack one on the other, selected area diffraction is used to distinguish contentious cases.

These combined analysis show that our ink mostly consists of SLGs, Bi-Layers (BLG) and FLGs, with lateral size~300-1000nm. We find that~35% SLGs are larger than 300nm (Figure 2d); ~40% BLGs are larger than 350nm (Figure 2e); ~55% FLGs are larger than 450nm (Figure 2f). In particular, we have 33% SLG with c~0.11g/L. Previous works on LPE of graphene in NMP reported up to~28% SLG for c~0.18g/L[58] and ~21% for c~1.8g/L.[94] Ref.[57] also reported exfoliation of intercalated graphite in NMP yielding~20% SLGs for c~0.01g/L. Thus our ink has higher SLG yield with respect to previous works, but lower c than ref.[94] This higher c was achieved by long time (up to 460h) ultrasonication.[94] However Ref.[94] reported defect formation and reduction of size as a result. Our combination of low-power sonication (<25W) followed by ultracentrifugation is ideal to obtain high yield of defect-free SLGs.

Stable dispersions require the Gibbs free energy of mixing, ΔG_{mix}, to be zero or negative,[95] where $\Delta G_{mix} = \Delta H_{mix} - K\Delta S_{mix}$, K being the temperature, ΔH_{mix} the enthalpy of mixing and and ΔS_{mix} the entropy change in the mixing process.[55,95] For graphene and nanotubes, ΔS_{mix} is small.[55,96] Therefore, for dispersion and stabilization of graphene in solvents, ΔH_{mix} needs to be very small. This can be achieved by choosing a solvent whose surface energy is very close to that of graphene.[55] The surface energy of NMP satisfies this requirement and allows efficient exfoliation of graphite. Graphite can also be efficiently exfoliated in water with the use of bile salt surfactants. Ref.[97] reported~20%SLGs and c~0.3g/L SLGs, while Ref.[59] reported~60% SLGs for c~0.012g/L. The yield can be increased up to~80% if combined with density gradient ultracentrifugation.[60] The flake size of LPE graphene in water-surfactant dispersions is on average smaller(~200nm,[97] ~30nm[59]) than thus far reported for NMP(~1μm[55,58]). The viscosity at room temperature of NMP (1.7mPas[86]) is higher than water (~1mPas[86]). Larger flakes dispersed in a higher viscosity medium (such as NMP) experience higher frictional force[98,99] and sedimentation coefficient[99,100] that make it more difficult for FLGs to sediment during ultracentrifugation. This reduces the yield of SLGs in NMP compared to water.

Figure 3a plots a typical Raman spectrum of the ink dispensed on Si/SiO$_2$ and annealed at 170°C to remove NMP. Besides the G and 2D peaks, it shows significant D and D' intensities and the combination mode D+D'$\sim$2950cm^{-1}. The G peak corresponds to the E$_{2g}$ phonon at the Brillouin zone centre. The D peak is due to the breathing modes of sp^2 rings and requires a defect for its activation by double resonance (DR).[93,101,102] The 2D peak is the second order of the D peak. This is a single band in SLG,[93] whereas it splits in four in BLG, reflecting the evolution of the band structure.[93] The 2D peak is always seen, even when no D peak is present, since no defects are required for the activation of two phonons with the same momentum, one backscattering from the other.[93] DR can also happen intra-valley, *i.e.* connecting two points belonging to the same cone around **K** or **K'**.[101–103] This gives the D' peak. The 2D' is the second order of the D' peak.

We assign the D and D' peaks to the edges of the sub-micrometer flakes,[104] rather than to the presence of a large amount of disorder within them. This is further supported by the plot of the G peak dispersion, Disp(G)(Figure 3b) (see Methods). In disordered carbons Pos(G) increases as the excitation wavelength decreases, from IR to UV,[101] thus Disp(G) increases with disorder.[101,105] The full width at half maximum of the G peak, FWHM(G), always increases with disorder.[106,107] Thus, combining I(D)/I(G), FWHM(G) and Disp(G) allows us to discriminate between disorder localized at the edges, and disorder in the bulk of the samples. In the latter case, to higher I(D)/I(G) would correspond higher FWHM(G) and Disp(G). Figure 4 a,b) show that Disp(G), I(D)/I(G) and FWHM(G) are not correlated, a clear indication that the major contribution to the D peak comes from the sample edges. Also, Disp(G) is nearly zero for all samples, compared to the values bigger than 0.1cm^{-1}/nm expected for disordered carbons,[105,108] another indication of the lack of large structural disorder within our flakes. The distribution of Pos(2D), shown in Figure 3d, has two maxima$\sim$2692 and 2705cm^{-1}, similar to FWHM(2D) (Figure 3e). This is consistent with the samples being a distribution of SLG, BLG and FLGs, but with a significant fraction of SLGs. We note that for the flakes with the smallest Pos(2D) and FWHM(2D), the ratio of the 2D and G integrated areas, A(2D)/A(G), is at most 3.5, implying a doping of at least 10^{13}cm^{-2}.[109–111]

We now estimate the η, ρ and γ for our graphene-ink, in order to check its viability. η can be

1
2
3
4
5
6
7
8
9
10
11
12
13
14
15
16
17
18
19
20
21
22
23
24
25
26
27
28
29
30
31
32
33
34
35
36
37
38
39
40
41
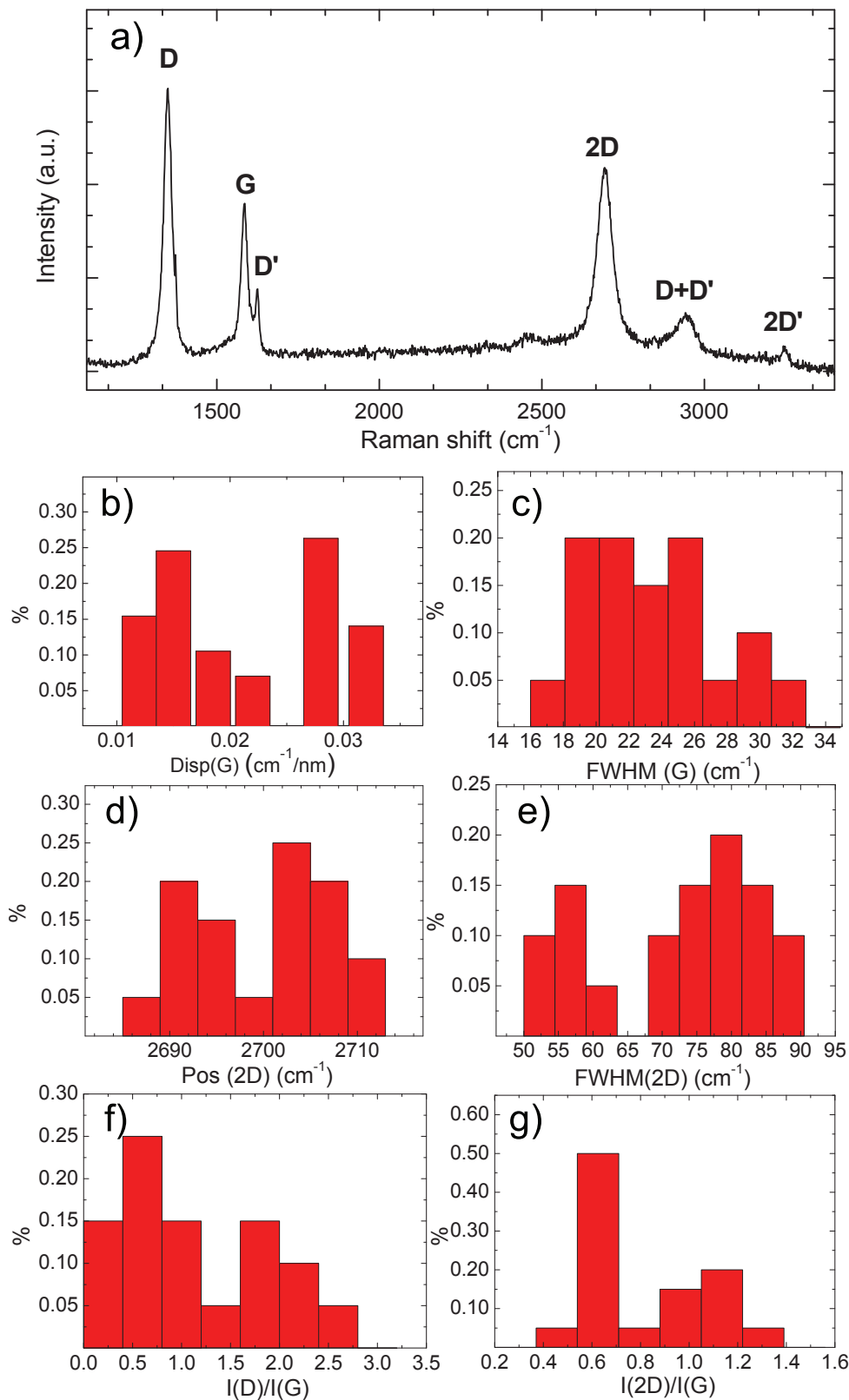42
43
44
45
46
47
48
49
50
51
52
53
54
55
56
57
58
59
60

Figure 3: a) Raman spectrum of graphene-ink deposited on Si/SiO$_2$ at 514.5nm excitation. Distribution of b) Disp(G), c) I(D)/I(G), d) FWHM(G), e) Pos(2D), f) FWHM(2D), g) A(2D)/A(G).
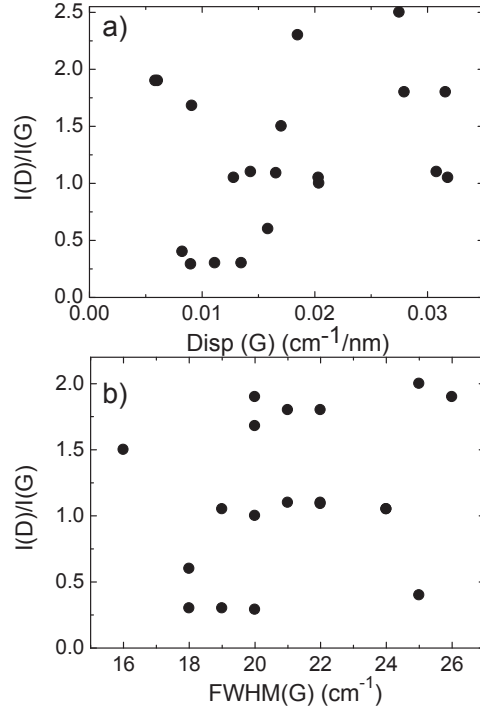
10

Figure 4: a) I(D)/I(G) as function of Disp(G), b) I(D)/I(G) as function of FWHM(G) measured on flakes of our ink deposited on Si/SiO$_2$.

evaluated as $\eta = \eta_0(1+2.5\phi)$,[82,112] where η_0 is the viscosity of the pure solvent and ϕ the volume fraction of particles in the dispersion. We assume $\eta_0 = \eta_{NMP} \sim 0.8$mPas, the viscosity of pure NMP at $\sim 80°$C[86,113] (the Temperature of the drops ejected from our printer[114]). We take $\phi = 1 - \frac{Vol_{NMP}}{Vol_{ink}}$, where Vol$_{NMP}$ [~ 0.972 mm^3] is the volume of 1mg pure NMP and Vol$_{ink}$ [~ 1.07 mm^3] is the volume of 1mg of our ink, both measured by a micropipette (± 2nL precision), at room temperature and pressure. We thus get $\phi \sim 0.1$, and $\eta \sim 0.96$mPas. We determine $\rho \sim 1.13$gcm^{-3} from the average weight over 20 measurements of 100μl of ink, and derive $\gamma \sim 50$mJ m^{-2} from tensiometer measurements. Given these parameters, and our nozzle diameter$\sim 50\mu$m, we get Z$\sim \frac{\sqrt{\gamma\rho a}}{\eta} \sim 2$, which falls within the range suitable for printing,[75,76] but close to the lower boundary of allowed Z.[75–77] On one hand, our ink has higher viscosity compared to that of usual printable inks,[82,112] implying a lower probability of secondary drops ejection.[75,82,112] On the other hand, high viscosity may generate nanoparticle re-aggregation.[112]

11

Ink-jet printed features

The final layout of printed nano-particle inks depends on the substrate SE,[21,23] as well as ink viscosity and surface tension.[21]

To investigate the influence of surface treatments, we print our ink on pristine, HMDS coated and O_2 plasma treated Si/SiO$_2$. A modified Epson Stylus 1500 ink-jet printer with a S020049 cartridge is used to print the dispersions under a constant nitrogen flow, followed by annealing at 170°C for 5 minutes to remove the NMP. The nozzle is placed$\sim$1mm above the substrate. HMDS is deposited by spin coating for 40s at 1000rpm, followed by annealing at 80°C for 2 min. Alternatively the substrates are cleaned by a RF O_2 plasma at 200W and 4×10^{-1} Torr for 2 min.

We use optical micrographs to visualize the ink-jet printed drops, Figure 5a,b,c. The bright green/blue color of the printed features is due to the use of dark field imaging. These reveal that HMDS constrains the drops to 90μm diameter (Figure 5c), smaller than on the other substrates ($\sim$100μm and $\sim$150μm for pristine, Figure 5b, and plasma treated SiO$_2$,Figure 5a). As discussed above, we use NMP as solvent to reduce the coffee ring effect compared to low boiling point solvents (e.g. water, chloroform).[18,82,84] However, we still observe coffee-rings when printing on pristine SiO$_2$ (Figure 5b), while Figure 5c reveals a higher flake uniformity, and no coffee-rings on HMDS treated SiO$_2$. Thus, HMDS appears to prevent coffee-rings. To understand this, we measure the substrates SE and investigate the printed stripes morphology, before and after surface treatment.

We utilize contact angle analysis to estimate the substrate surface tension and SE. θ_C depends on the liquid surface tension[79-81] and the substrate critical surface tension,[79-81] according to the the Young's relation[79,81,115] γ_{SV}-γ_{SL}-$\gamma_{LV}\cos\theta_C$=0, where γ_{SV} [mJ m^{-2}] is the solid-vapor surface tension, γ_{SL} is the solid-liquid surface tension and γ_{LV} is the liquid-vapor surface tension. Figure 5d is a Scanning Electron Microscope (SEM) micrograph of a representative printed pattern showing the viability of ink-jet printing to fabricate complex layouts.

Figure 6a,b show ink drops printed onto pristine and HMDS treated Si/SiO$_2$, with θ_C $\sim$6° and$\sim$65°, indicating that the pristine substrate SE is modified following HMDS treatment. γ_{LV}
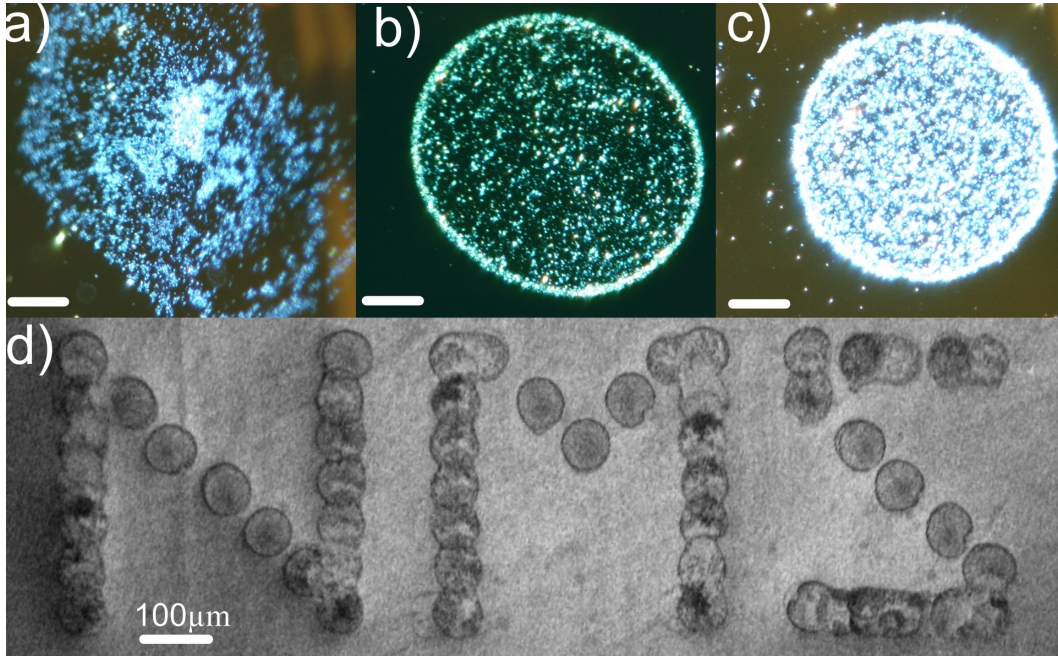
Figure 5: Dark field optical micrograph of inkjet printed drops on a) plasma cleaned, b) pristine and c) HMDS treated substrate. Scale is 20μm. d) SEM micrograph of drops printed in a pattern.
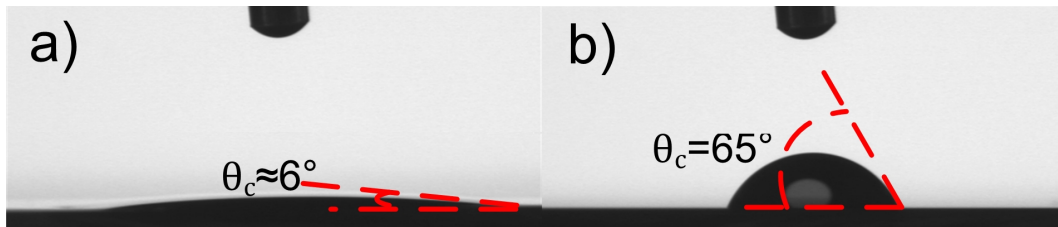

Figure 6: Images of water drops dispensed on a) pristine and b) HMDS teated Si/SiO$_2$ substrates

was measured$\sim$73mJ m^{-2} in Ref.[116] for DI water, whereas $\gamma_{SV} \sim$143.50mJ m^{-2} and$\sim$20mJ m^{-2} were reported for pristine[116] and HMDS treated[116] Si/SiO$_2$ substrates. Consequently, $\gamma_{SL} \sim$73mJ m^{-2} and $\sim$29mJ m^{-2} for pristine and HMDS treated Si/SiO$_2$, respectively. A higher γ_{SL} implies a higher SE.[80,117] Indeed, our γ_{SL} correspond to SEs$\sim$120 and$\sim$50mJ m^{-2} for pristine and HMDS treated Si/SiO$_2$. A small θ_C results in the drop rapid spreading on the substrate,[79] as seen in pristine SiO$_2$. On the other hand, HMDS provides higher θ_C, since it lowers γ_{SL} (thus the substrate SE), therefore reducing the wettability.[80,117]

When ink-jet printing stripes, the inter-drop (i.e. centre to centre) distance is an important parameter.[118] For a large distance, individual drops are deposited on the substrate.[75,82,118] As the inter-drop distance decreases, these merge into a line.[118] Thus, in order to obtain a continuous line we need an inter-drop distance smaller than the drop diameter.[118] On the other hand, Refs.[82,112] reported that a very small inter-drop distance can result in particle aggregation on the substrate, giving a non-uniform stripe (i.e. irregular edges). We thus select an inter-drop distance suitable to have continuous lines, avoiding at the same time non-uniformities and irregular edges.

Figure 7a,b,c are optical images of printed stripes on pristine, O$_2$ plasma treated and HMDS treated Si/SiO$_2$, whereas Figure 7d,e,f plot the respective Atomic Force Microscope (AFM) topographies. The stripe in Figure 7a is$\sim$100-110μm wide, has an average thickness$\sim$70nm and an irregular flake distribution, with aggregation of flakes. That in Figure 7b is wider ($\sim$130-140μm), with aggregates at the edges, and an average thickness$\sim$55nm. The stripe in Figure 7c has a more uniform and regular distribution of flakes, having$\sim$85-90μm width and$\sim$90nm average thickness. The width narrows going from the O$_2$ plasma treated to the HMDS treated Si/SiO$_2$, due to the SE decrease. Figure 7d,e show stripes with voids and irregular flake distribution, with R$_z \sim$30-40nm. Figure 7f presents a more homogeneous network with R$_z \sim$15nm. Thus, R$_z$ is lower when θ_C is higher, because the poor wettability of drops with higher θ_C reduces the stripe diameter (as shown in Figure 7a,b,c), confining the flakes onto a smaller area. The uniformity of stripes printed on the HMDS treated substrate corroborates the above considerations on the SE changes. In fact, the presence of silane groups in the molecular structure of HMDS[85] acts as promoter of metallic par-

ticles adhesion to the substrate.[85,119] Analogously, HMDS may promote the adhesion of graphene

flakes to the substrate, thus favoring the formation of a regular network.
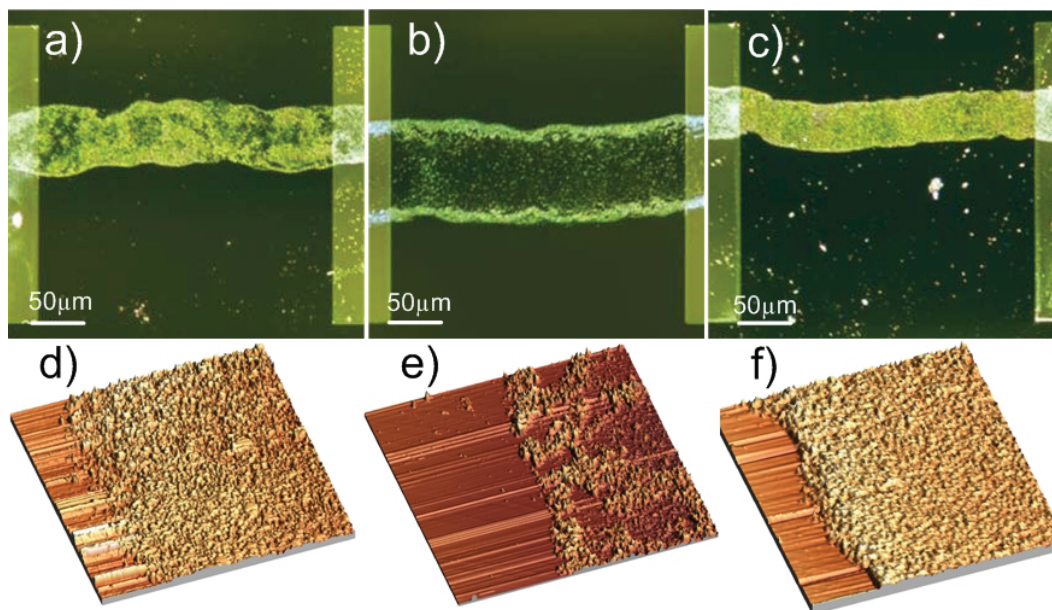

Figure 7: Optical micrograph of ink-jet printed stripes on a) pristine, b) O_2 and c) HMDS treated substrates.d,e,f) AFM images of a,b,c, respectively.

Figure 8a compares a typical Raman spectrum of a flake in the ink, with a measurement on

the first stripe and on a stripe 90 nm thick, after 30 printing repetitions. Spectra are acquired after

annealing at $170°C$ to remove the NMP. Figure 8b,c,d,e,f,g and Figure 9 compare the Pos(2D),

FWHM(2D) and Disp(G) distributions. The data show that the first stripe has very similar char-

acteristics to the ink, as expected. However, the spectra after 90 repetitions show a Pos(2D) and

FWHM(2D) distributions more typical of a multi-layer sample, having lost any direct signature of

SLG. Note however that the 2D peak shape, even for the 90nm stripe, remains distinctly different

from that of graphite. A similar aggregation of flakes was previously observed for thick films de-

rived from graphene solutions.[55] In all cases Disp(G) remains similar, and very low, again showing

the lack of large amounts of defects within the flakes.

1
2
3
4
5
6
7
8
9
10
11
12
13
14
15
16
17
18
19
20
21
22
23
24
25
26
27
28
29
30
31
32
33
34
35
36
37
38
39
40
41
42
43
44
45
46
47
48
49
50
51
52
53
54
55
56
57
58
59
60
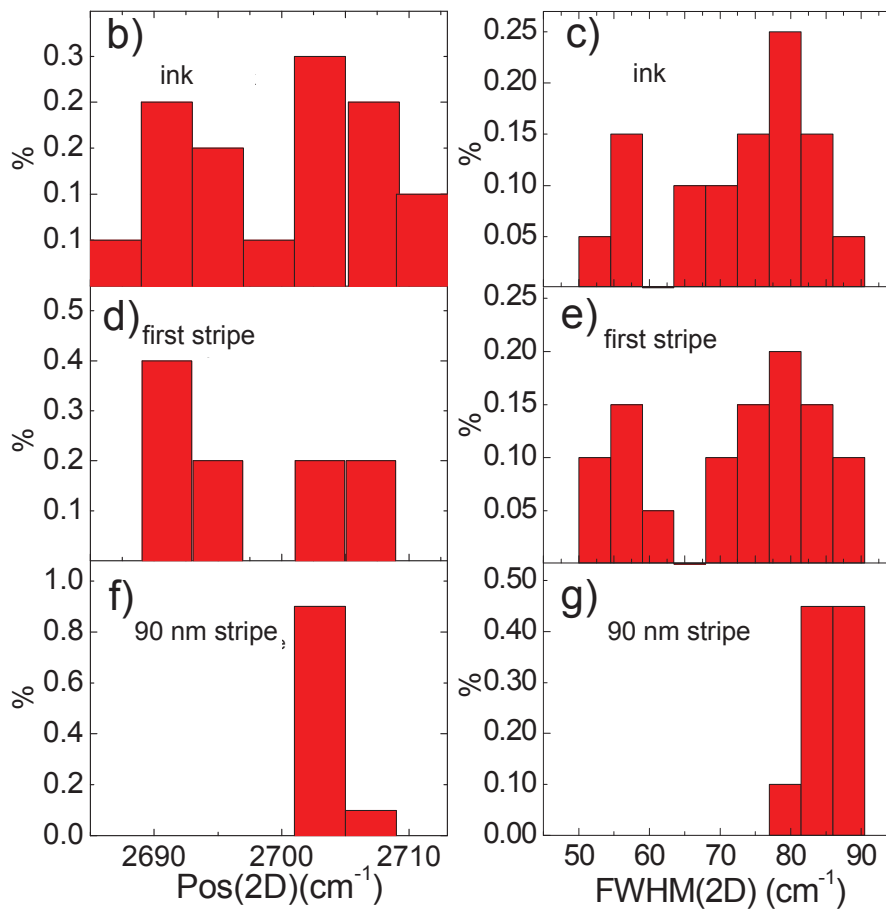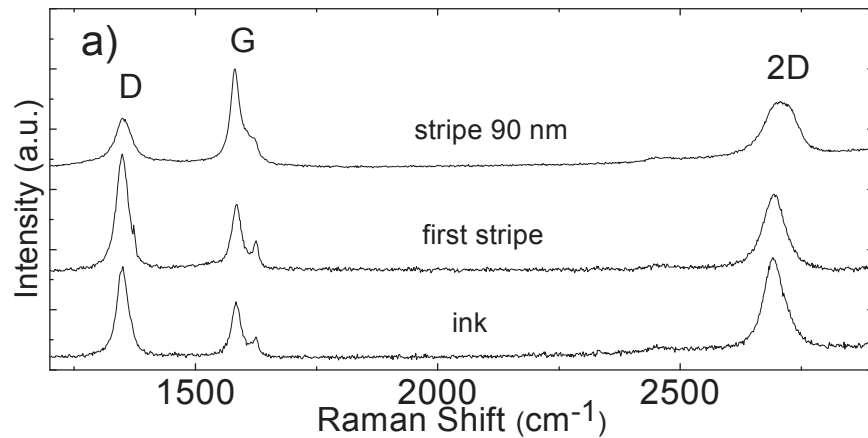
Figure 8: a) Typical Raman spectrum of individual flakes in the ink, compared with spectra measured on the first stripe and on a stripe 90nm thick. Pos(2D) and FWHM(2D) distributions for b,c) ink; d,e) fist stripe; f,g) 90nm thick stripe.
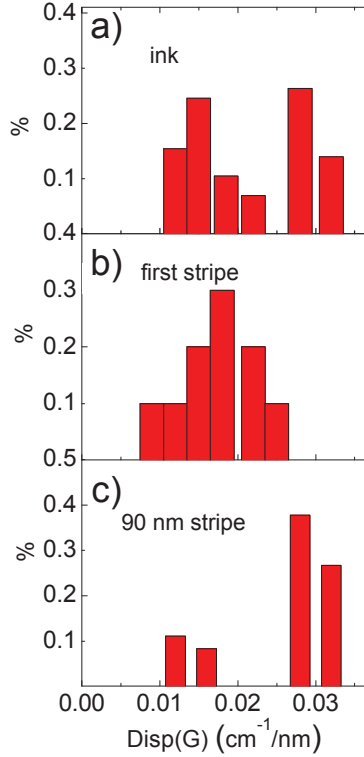
Figure 9: Distribution of Disp(G) for a) ink, b) fist stripe, c) 90nm thick stripe

Transparent and conductive patterns

We now investigate the viability of our ink to print transparent and conductive patterns. We characterize the sheet resistance R_s [Ω/□] and Transmittance T [%] of our stripes when placed on a transparent substrate. We thus use pristine, O_2 and HMDS treated borosilicate glass, with R_z<15nm similar to SiO_2 on Si, but with T~99% (Pyrex 7740-Polished Prime Grade).

Figure 10a shows that for our stripes the thickness (t) increases linearly as a function of printing repetitions, with a slope defined by the surface treatment. Figure 10b plots the four-probe measured R_s (see Methods) as a function of t. For large t, R_s settles to~34kΩ/□, ~500kΩ/□, and~10^5kΩ/□ for HMDS treated, pristine and O_2 treated glass, respectively. For t<20nm, R_s increase for all substrates. For a thin film, $R_s = (\sigma\, t)^{-1}$, where σ [S/m] is the conductivity.[120] Thus, from Figure 10b and $\sigma=(R_s\, t)^{-1}$, we get the data in Figure 10c. σ is constant for t>20nm, in the case of HMDS treated, pristine and plasma treated glass, with an averageσ ~10^2S/m,~30S/m, and~10^{-1}S/m, respectively. Thus, stripes on HMDS treated glass have an higher σ combined

1
2
3
4
5
6
7
8
9
10
11
12
13
14
15
16
17
18
19
20
21
22
23
24
25
26
27
28
29
30
31
32
33
34
35
36
37
38
39
40
41
42
43
44
45
46
47
48
49
50
51
52
53
54
55
56
57
58
59
60

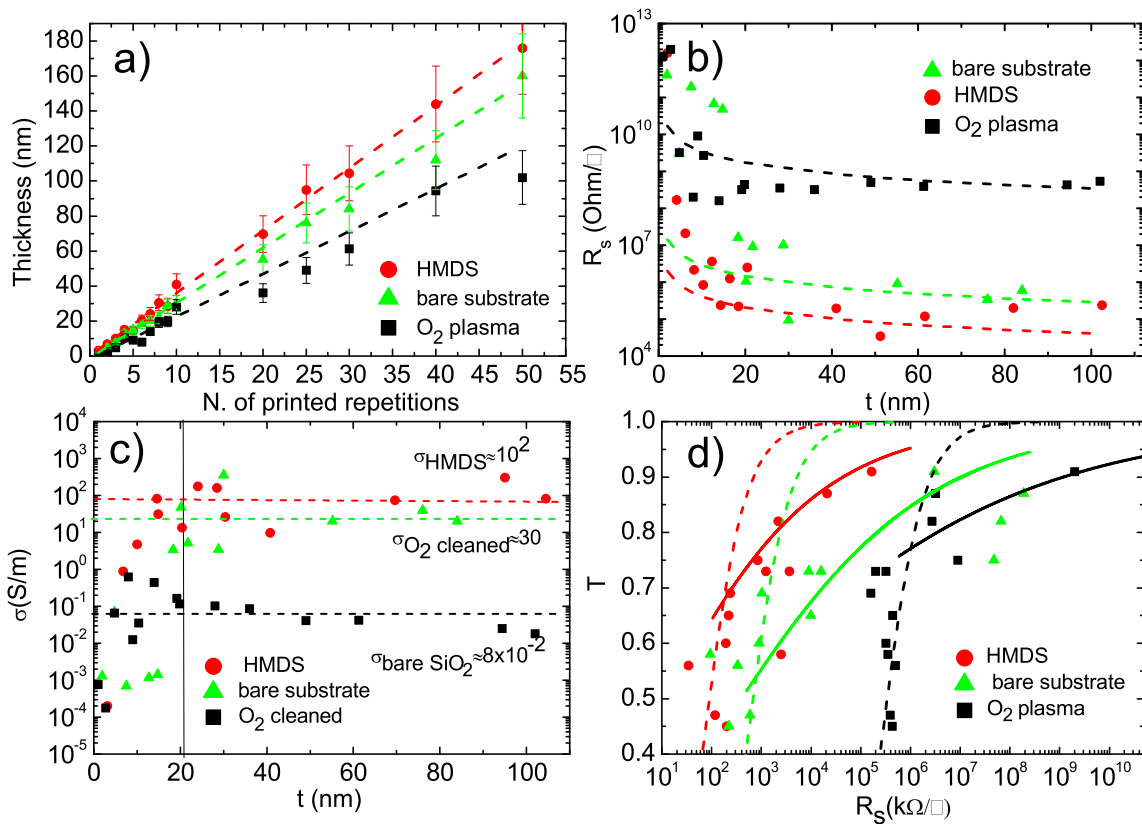
Figure 10: a) Thickness as a function of printing repetitions. b,c) R_s, σ as a function of thickness. d) T as a function of R_s for HMDS coated (red dots), O_2 plasma treated (green triangles) and pristine (black squares) substrates

with a more regular network of flakes, compared to the other two substrates. When t<20nm, σ

decreases for all substrates. A similar trend was reported for CNT films on SiO_2 (produced by vac-

uum filtration),[121,122] ink-jet printed CNT patterns on SiO_2,[29,30] graphene films on SiO_2,[123,124]

and Polyethylene-terephthalate(PET),[123,124] as well as Ag nanowire films, produced by vacuum

filtration on SiO_2.[123] Refs.[121–124] explained this decrease of σ for small t, due to percolation.

The percolation theory[125] predicts σ, for a network of conductive particles, to scale as:[125]

$$\sigma \propto (X - X_c)^{\beta} \tag{1}$$

where X [μg/mm^2] is the concentration of conductive particles per unit area, X_c [μg/mm^2] is the

critical concentration of flakes corresponding to the percolation threshold and β is the percolation

exponent. Eq. (1) can be rewritten in terms of t, rather than X [121] as:

$$\sigma \propto (t - t_c)^{\varepsilon} \tag{2}$$

where t_c is the critical thickness and ε is the percolation exponent. Figure 10c shows two regimes

for σ as a function of t: a percolative linear behavior for t<20nm and a constant σ_{bulk} for t>20nm.

Such regimes can be explained considering that our films stop behaving like bulk materials below

a critical thickness (t_{min}), entering the percolation region.

The exponent ε can be estimated by a linear fit of the $\log_{10}$ plot of σ vs t, in the percolation

region (t<20nm),Figure 11. We get $\varepsilon \sim 4$ for stripes on HMDS treated and pristine glass, while

$\varepsilon \sim 3$ for O_2 treated glass. These values indicate percolation, as reported by Refs.[123,126–128] for

networks with various geometries. ε is expected to increase with particle size[127,128] and decrease

with X_c.[127,128] Assuming a similar particle size, since the same ink is used for all cases, we deduce

that $\varepsilon \sim 4$ points to a smaller X_c than $\varepsilon \sim 3$. This indicates formation of a more uniform network on

HMDS treated and pristine glass compared to O_2 treated glass.

We also determine the minimum concentration necessary to achieve the bulk conductivity

regime. To do this we assume X$\gg$X$_C$, because the bulk regime needs a tight network of intercon-
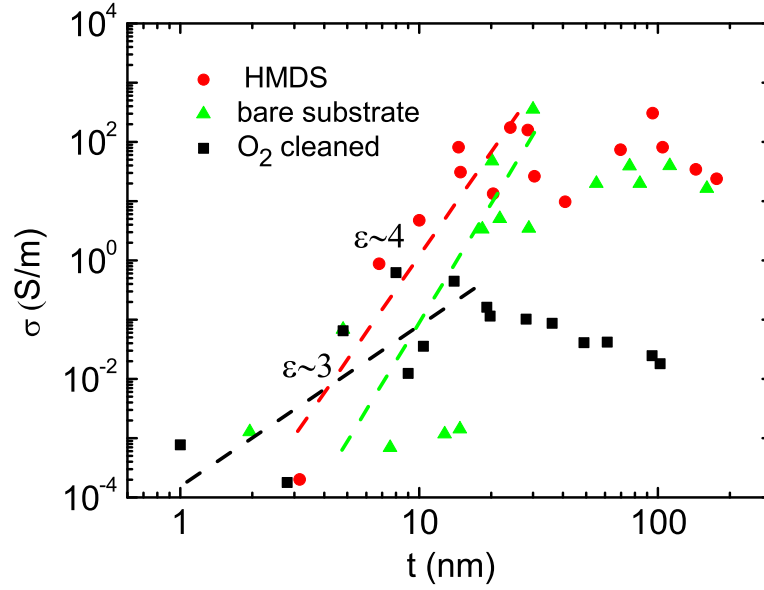
19

Figure 11: Conductivity as a function of film thickness, in logarithmic scale, for stripes printed on HMDS treated (red dots), O_2 treated (green triangles) and pristine (black squares) substrates. Lines are fits in the percolation regime of conductivity.

nected flakes.[123,126,129] Given our $c \sim 0.11$g/L, volume per printed drop~ 10nL,[114] and a dried drop size on the three substrates of$\sim 90, 100, 130 \mu$m, we estimate $X \sim 4 \times 10^{-2}, \sim 10^{-2}$ and$\sim 0.7 \times 10^{-2} \mu$g/mm^2 for stripes printed on HMDS, pristine and plasma treated glass, respectively. Consequently, from Eq. (1), σ for stripes printed on HMDS treated glass ($\sigma \sim 10^2$S/m) is higher than on pristine ($\sigma \sim 40$S/m) and plasma treated glass($\sigma \sim 0.1$S/m).

Figure 10d plots T as a function of R_s. The dashed lines are a plot of the relation T$=\left(1 + \frac{Z_0 \, G_0}{2R_s \sigma_{bulk}}\right)^{-2}$ expected for graphene-ink stripes with σ_{bulk} conductivity, where $Z_0 = 377\Omega$ is the free-space impedance, $G_0 \sim 6 \times 10^{-5} \Omega^{-1}$ is the universal optical conductance of graphene.[130] The solid lines are a plot of T$=\left[1 + \frac{1}{\Pi} \left(\frac{Z_0}{R_s}\right)^{1/(\varepsilon+1)}\right]^{-2}$ expected for stripes in the percolative regime,[123] where Π is the percolative Figure of Merit $\Pi = 2 \left[\frac{\sigma_{bulk}/G_0}{(Z_0 \, t_{min} \, G_0)^\varepsilon}\right]^{1/(\varepsilon+1)}$. Our experimental T deviates from the dashed lines for T>75%. We assign this to the percolative regime, with σ_{DC} deviating from a bulk-like behavior. Also in this case, printing on HMDS treated glass gives the highest T for a given R_s.

Ink jet printed devices

Ink-jet printed TFTs based on organic semiconducting polymers have been widely investigated.[15,131,132] The current state of the art devices have μ ranging from 0.01 to $\sim$0.5cm^{2}V^{-1}s^{-1}, with ON/OFF ratios up to 10^5.[131–133] Several inkjet printed TFTs using various carbon nanomaterials have been reported. For example, fullerene-based TFTs were discussed in Refs.,[134,135] with μ up to 0.01cm^{2}V^{-1}s^{-1} and an ON/OFF ratio<10. TFTs printed from SWNT-based inks have been presented by several groups.[27–29,31,32] The highest μ reported thus far is $\sim$50cm^{2}V^{-1}s^{-1} combined with an ON/OFF ratio 10^3, but measured at 10^{-6} Torr and 100K.[32] Ink-jet printed TFTs from GO-based inks were discussed in Refs.,[72,73] with μ up to $\sim$90cm^{2}V^{-1}s^{-1} for an ON/OFF ratio of 10 (measured at room conditions), after GO reduction.
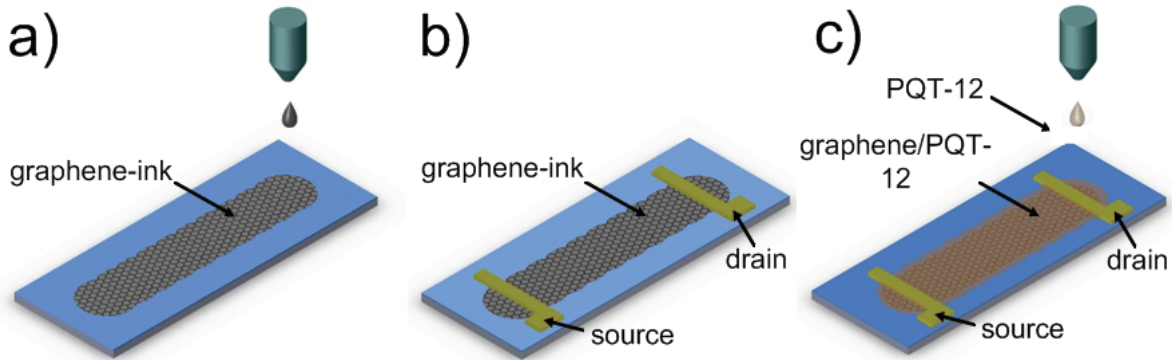

Figure 12: a) Graphene-ink on Si/SiO$_2$. b) Two Cr-Au pads define the source and drain contacts. c) A layer of Poly[5,5'-bis(3-dodecyl-2-thienyl)-2,2'-bithiophene] (PQT-12) is printed on top.

We print our TFTs as for Figure 12a, and contact them with chromium-gold source and drain pads (Figure 12b). The transfer characteristics are measured (at room conditions) at different drain voltages (V$_d$=-2,-4,-8V). We get μ from the slope of the transfer-characteristic according to $\mu = \frac{L}{W \, C_i \, V_d} \frac{dI_d}{dV_g}$, where L [$\mu$m] and W [$\mu$m] are the channel length and width respectively, C$_i$ is the gate dielectric capacitance ($\sim$10nF/cm^2).[136] This corresponds to $\mu \sim$95cm^{2}V^{-1}s^{-1} and ON/OFF ratio$\sim$10 at V$_d$=-8V, comparable to those reported in Ref.[73] for ink-jet printed RGO TFTs. μ in our devices is almost four times higher than printed fullerene-based TFTs[134,135] (for the same ON/OFF ratio) and more than two orders of magnitude higher than that reported for ink-jet printed

SWNTs[27,29] (for a on/off ratio of 10). However, the ON/OFF ratio in our TFTs is lower than the state of the art for SWNTs (but measured at 10^{-6} Torr and 100K) at similar μ.[32] We note that ink-jet printed electronics requires high μ at room conditions.[11,18] So far SWNT ink-jet printed devices measured at room conditions have μ no larger than $\sim 1 cm^2 V^{-1} s^{-1}$ (at ON/OFF ratio$\sim$10),[29] which is two orders of magnitude smaller than our graphene ink-jet printed TFTs.
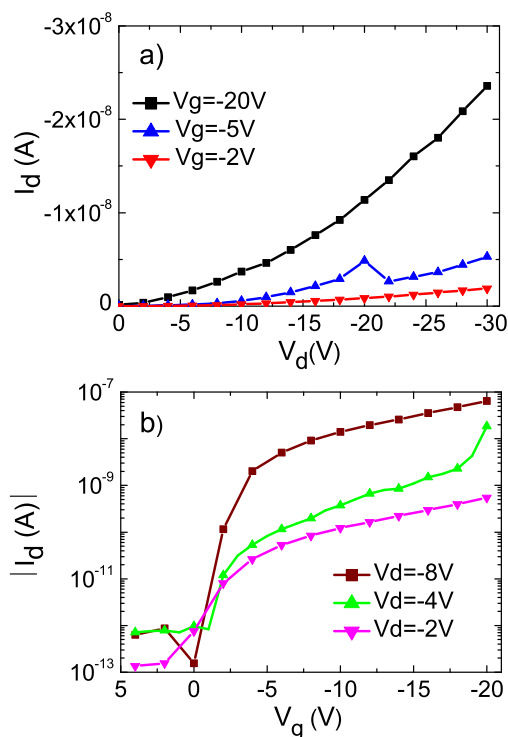
Figure 13: a) Output characteristics and b) transfer characteristic of an ink-jet printed graphene/PQT TFT.

Organic semiconducting inks[131–133] suffer from low μ, limited by variable range hopping of charges between the isolated polymer chains.[137] The overall charge conduction in crystalline organic semiconducting thin films is determined by both intra-chain and inter-chain charge transport.[138] The intrachain transport is much faster than inter-chain hopping.[137,138] Many groups have tried to improve interchain hopping.[27,28,139,140] Ref.[139] proposed a chemical modification of the semiconducting organic ink by electron acceptor, while embedding Au nano-particles in the semiconducting organic ink was proposed in Ref.[140] Embedding SWNTs in the semiconducting ink allowed us to get $\mu \sim 0.07 cm^2 V^{-1} s^{-1}$ at room conditions.[27,28]

We combine our graphene-ink with one of the most common organic polymer in ink-jet printing, Poly[5,5'-bis(3-dodecyl-2-thienyl)-2,2'-bithiophene] (PQT-12)[131–133] in order to investigate its viability as interchain hopping enhancer. PQT-12 is widely used due to the higher environmental stability (up to 300 days at room conditions[141]), with respect to other organic semiconducting inks.[140,141] Graphene can bridge the polymer chains, allowing more efficient charge transport.

We fabricate a graphene/PQT-12 TFT following the steps shown in Figure 12a,b,c. Figure 13a plots its output characteristics at V_g=-2,-5,-20 V. For each V_g, V_d is swept from 0 to -30 V in steps of 2V. At V_d=-8V, we get $\mu \sim$0.2cm^{2}V^{-1}s^{-1} and an ON/OFF ratio$\sim$4$\times$10^5. This μ is about ten times that for ink-jet printed SWNTs/PQT-12 TFTs[27,28] at an ON/OFF ratio$\sim$10^5. When compared to pure organic semiconducting polymers, our μ is 20 times higher than ink-jet printed PQT-12,[132,133] and twice the highest reported μ for ink-jet printed TFT made of pure (Poly(2,5-bis(3-tetradecyllthiophen-2-yl)thieno[3,2-b]thiophene).[18,140,142,143] Thus, the combination of graphene- and organic semiconducting- inks is promising for high performance printed electronics.

Conclusions

We demonstrated ink-jet printing of graphene. Liquid phase exfoliated graphene is an ideal and low cost material for the fabrication of transparent conductive inks. Our graphene-ink was used to print TFTs with μ up to $\sim$95cm^{2}V^{-1}s^{-1}. It was also combined with PQT-12 to fabricate devices with $\mu \sim 0.2 cm^2$V^{-1}s^{-1} and ON/OFF ratios$\sim$4$\times$10^5. This demonstrates the viability of graphene-inks for flexible and transparent electronics.

Methods

Raman spectroscopy

The centrifuged dispersions are diluted and drop-cast onto a Si wafer with 300nm thermally grown SiO$_2$ (LDB Technologies ltd.). These samples are then used for Raman measurements,

collected with a Renishaw 1000 at 457, 514.5 and 633nm and a $100\times$ objective, with an incident power of~1mW. The G peak dispersion is defined as $\text{Disp(G)} = \Delta Pos(G)/\Delta\lambda_{\text{L}}$, where λ_L is the laser excitation wavelength. Disp(G) is generated from the linear fit the plot of Pos(G) as a function of the laser excitation wavelength.

Contact angle and surface tension measurements

A KSV CAM200 stage is used for contact angle and surface tension measurements. The contact angle is measured by dispensing 1μl ultrapure DI water on the substrates and measuring the angle at which the ink interface meets the solid surface. The surface tension is measured by the DuNouy-Padday technique. [144] This consists in using a rod few millimeters diameter immersed in the dispersion, followed by pull out. The rod is attached to a scale or balance via a thin metal hook that measures the maximum pull force. This is recorded as the probe is first immersed 1mm into the solution and then slowly withdrawn from the interface.

Optical transmittance

The transmittance is measured on samples ink-jet printed on borosilicate glass (Pyrex 7740 - Polished Prime Grade) followed by annealing at $170°$C for 1h by scanning a 514.5nm laser beam onto the sample at 100μm steps. The transmitted beam is measured with a photodiode. An optical microscope equipped with $100\times$ long-distance objective focuses the laser on the sample down to a spot size of~2μm (incident power on the sample~8mW). The transmitted power intensity is measured by a Ophir Nova II power meter with 0.1μW resolution.

Electrical measurements

Electrical measurements to characterize the printed devices are performed using a cascade attoguard probe station equipped with an Agilent Semiconductor Parameter Analyzer 4156C. The integration time is set to 500μs and the delay time is set to 50ms to ensure that no transient instabilities in the current occur.

Acknowledgements

References

[1] Cao, Q.; Kim, H.-S.; Pimparkar, N.; Kulkarni, J. P.; Wang, C.; Shim, M.; Roy, K.; Alam, M. A.; Rogers, J. A. Medium-scale carbon nanotube thin-film integrated circuits on flexible plastic substrates. *Nature* **2008**, *454*, 495-500.

[2] Zhou, L.; Wanga, A.; Wu, S.-C.; Sun, J.; Park, S.; Jackson, T. N. All-organic active matrix flexible display. *Appl. Phys. Lett.* **2006**, *88*, 083502-3.

[3] Ota, I.; Ohnishi, J.; Yoshiyama, M. Electrophoretic image display (EPID) panel. *Proc. IEEE* **1973**, *61*, 832-836.

[4] Gelinck, G. H.; Huitema, H. E. A.; van Veenendaal, E.; Cantatore, E.; Schrijnemakers, L.; van der Putten, J. B. P. H.; Geuns, T. C. T.; Beenhakkers, M.; Giesbers, J. B.; Huisman, B.-H.; Meijer, E. J.; Benito, E. M.; Touwslager, F. J.; Marsman, A. W.; van Rens, B. J. E.; de Leeuw, D. M. Flexible active-matrix displays and shift registers based on solution-processed organic transistors. *Nat. Mater.* **2004**, *3*,106-110.

[5] Sekitani, T.; Yokota, T.; Zschieschang, U.; Klauk, H.; Bauer, S.; Takeuchi, K.; Takamiya, M.; Sakurai, T.; Someya, T. Organic Nonvolatile Memory Transistors for Flexible Sensor Arrays. *Science* **2009**,*326*,1516-1519.

[6] Myny, K.; Steudel, S.; Vicca, P.; Beenhakkers, M. J.; van Aerle, N. A. J. M.; Gelinck, G. H.; Genoe, J.; Dehaene, W.; Heremans, P. Plastic circuits and tags for 13.56ăMHz radio-frequency communication. *Solid state Electron.* **2009**, *53*, 1220-1226.

[7] Granqvist, C. G. Transparent conductors as solar energy materials: A panoramic review. *Sol. Energ. Mat. Sol. C.* **2007**, *91*,1529-1598.

[8] Yoon, J.; Baca, A. J.; Park, S.-I.; Elvikis, P.; Geddes, J. B.; Li, L.; Kim, R. H.; Xiao, J.; Wang, S.; Kim, T.-H. *et al.* Ultrathin silicon solar microcells for semitransparent, mechanically flexible and microconcentrator module designs. *Nat. Mater.* **2008**, *7*, 907-915.

[9] Schmied, B.; Gunther, J.; Klatt, C.; Kober, H.; Raemaekers, E. In *Smart Textiles*, STELLA - STretchable ELectronics for Large Area applications-A new technology for smart textiles, **2009**, *60*, 67-73.

[10] Kim, D; Jong-Hyun, A.; Hoon-Sik, K.; Keon Jae, L.; Tae-Ho, K.; Chang-Jae, Y.; Nuzzo, R. G.; Rogers, J. A. Complementary Logic Gates and Ring Oscillators on Plastic Substrates by Use of Printed Ribbons of Single-Crystalline Silicon. *IEEE Electr. Device L.* **2008**, *29*,73-76.

[11] Singh, T. B.; Sariciftci, N. S. Progress in plastic electronics devices. *Annu. Rev. Mater. Res.* **2006**, *36*, 199-230.

[12] Rogers, J. A.; Bao, Z.; Baldwin, K.; Dodabalapur, A.; Crone, B.; Raju, V. R.; Kuck, V.; Katz, H.; Amundson, K.; Ewing, J.; Drzaic, P.; Paper-like electronic displays: Large-area rubber-stamped plastic sheets of electronics and microencapsulated electrophoretic inks. *P. Natl. Acad. Sci. U.S.A.* **2001**, *98*, 4835-4840.

[13] Forrest, S. R. The path to ubiquitous and low-cost organic electronic appliances on plastic. *Nature* **2004**, *428*, 911-918.

[14] Bao, Z.; Rogers, J. A.; Katz, H. E. Printable organic and polymeric semiconducting materials and devices, *Journal of Materials Chemistry* **1999**, *9*, 1895-1904.

[15] Sirringhaus, H.; Kawase, T.; Friend, R. H.; Shimoda, T.; Inbasekaran, M.; Wu, W.; Woo,

E. P. High-resolution inkjet printing of all-polymer transistor circuits. *Science* **2000**, *290*, 2123-2126.

[16] Sun, Y. G.; Menard, E.; Rogers, J. A.; Kim, H. S.; Kim, S.; Chen, G.; Adesida, I.; Dettmer, R.; Cortez, R.; Tewksbury, A. Gigahertz operation in flexible transistors on plastic substrates. *Appl. Phys. Lett.* **2006**, *88*, 3.

[17] McAlpine, M. C.; Friedman, R. S.; Lieber, C. M. High-Performance Nanowire Electronics and Photonics and Nanoscale Patterning on Flexible Plastic Substrates. *Proc. IEEE* **2005**, *93*, 1357-1363.

[18] Singh, M.; Haverinen, H. M.; Dhagat, P.; Jabbour, G. E. Inkjet Printing - Process and Its Applications. *Adv. Mater.* **2010**, *22*, 673-685.

[19] Peumans, P.; Uchida, S.; Forrest, S. R. Efficient bulk heterojunction photovoltaic cells using small-molecular-weight organic thin films. *Nature* **2003**, *425*, 158-162.

[20] Servati, P.; Nathan, A. Functional pixel circuits for elastic AMOLED displays. *Proc. IEEE* **2005**, *93*, 1257-1264.

[21] DeGans, B. J.; Duineveld, P.; Schubert, U. Inkjet Printing of Polymers: State of the Art and Future Developments. *Adv. Mater.* **2004**, *16*, 203-213.

[22] Dong, H. M.; Carr, W. W.; Morris, J. F. An experimental study of drop-on-demand drop formation. *Phys. Fluids* **2006**, *18*, 16.

[23] Van Osch, T. H. J.; Perelaer, J.; de Laat, A. W. M.; Schubert, U. S. Inkjet printing of narrow conductive tracks on untreated polymeric substrates. *Adv. Mater.* **2008**, *20*, 343.

[24] Yoo, J. E.; Lee, K. S.; Garcia, A.; Tarver, J.; Gomez, E. D.; Baldwin, K.; Sun, Y.; Meng, H.; Nguyen, T.-Q.; Loo, Y.-L. Directly patternable, highly conducting polymers for broad applications in organic electronics. *Proc. Natl. Acad. Sci. U.S.A.* **2010**, *107*, 5712-5717.

[25] Shimoda, T.; Matsuki, Y.; Furusawa, M.; Aoki, T.; Yudasaka, I.; Tanaka, H.; Iwasawa, H.; Wang, D.; Miyasaka, M.; Takeuchi, Y. Solution-processed silicon films and transistors. *Nature* **2006**, *440*, 783-786.

[26] Noh, Y.-Y.; Cheng, X.; Sirringhaus, H.; Sohn, J. I.; Welland, M. E.; Kang,D. J. Ink-jet printed ZnO nanowire field effect transistors. *Appl. Phys. Lett.* **2007**, *91*, 043109-3.

[27] Beecher, P.; Servati, P.; Rozhin, A.; Colli, A.; Scardaci, V.; Pisana, S.; Hasan, T.; Flewitt, A. J.; Robertson, J.; Hsieh, G. W.; Li, F. M.; Nathan, A.; Ferrari, A. C.; Milne, W. I. Ink-jet printing of carbon nanotube thin film transistors. *J. Appl. Phys.* **2007**, *102*, 043710.

[28] Hsieh, G. W.; Li, F. M.; Beecher, P.; Nathan, A.; Wu, Y. L.; Ong, B. S.; Milne, W. I. High performance nanocomposite thin film transistors with bilayer carbon nanotube-polythiophene active channel by ink-jet printing. *J. Appl. Phys.* **2009**, *106*, 7.

[29] Takenobu, T.; Miura, N.; Lu, S.-Y.; Okimoto, H.; Asano, T.; Shiraishi, M.; Iwasa, Y. A. Ink-Jet Printing of a Single-Walled Carbon Nanotube Thin Film Transistor, *App. Phys. Expr.* **2009**, *2*, 025005.

[30] Okimoto, H.; Takenobu, T.; Yanagi, K.; Miyata, Y.; Shimotani, H.; Kataura, H.; Iwasa, Y. Tunable Carbon Nanotube Thin-Film Transistors Produced Exclusively via Inkjet Printing. *Adv. Mater.* **2010**, *22*, 3981-3986.

[31] Okimoto, H.; Takenobu, T.; Yanagi, K.; Miyata, Y.; Kataura, H.; Asano, T.; Iwasa,Y. Ink-Jet Printing of a Single-Walled Carbon Nanotube Thin Film Transistor. *J. J. App. Phys.* **2009**, *48*, 4.

[32] Ha, M.; Xia, Y.; Green, A. A.; Zhang, W.; Renn, M. J.; Kim, C. H.; Hersam, M. C.; Frisbie, C. D. Printed, Sub-3V Digital Circuits on Plastic from Aqueous Carbon Nanotube Inks. *ACS Nano* **2010**, *4*, 4388-4395.

[33] Luechinger, N.; Athanassiou, A. E. K.; Stark, W. J. Graphene-stabilized copper nanoparticles as an air-stable substitute for silver and gold in low-cost ink-jet printable electronics. *Nanotechnol.* **2008**, *19*, 445201.

[34] Geim, A. K.; Novoselov, K. S. The Rise of Graphene. *Nat. mater.* **2007**, *6*, 183-191.

[35] Novoselov, K. S.; Geim, A. K.; Morozov, S. V.; Jiang, D.; Zhang, Y.; Dubonos, S. V.; Grigorieva, I. V.; Firsov, A. A. Electric Field Effect in Atomically Thin Carbon Films. *Science* **2004**, *306*, 666-669.

[36] Charlier, J. C.; Eklund, P. C.; Zhu, J.; Ferrari A. C., In *Carbon Nanotubes, Topics Appl. Physics*; Jorio, A., Dresselhaus, G., Dresselhaus, M.S., Eds.; Springer-Verlag: Berlin Heidelberg **2008**; *111*, 673-709.

[37] Bonaccorso, F.; Sun, Z.; Hasan, T.; Ferrari, A. C. Graphene for Photonics and Optoelectronics. *Nat. Photon.* **2010**, *4*, 611-622.

[38] Lin, Y.-M.; Dimitrakopoulos, C.; Jenkins, K. A.; Farmer, D. B.; Chiu, H.-Y.; Grill, A.; Avouris, P. 100-GHz Transistors from Wafer-Scale Epitaxial Graphene. *Science* **2010**, *327*, 662.

[39] Sun, Z.; Hasan, T.; Torrisi, F.; Popa, D.; Privitera, G.; Wang, F.; Bonaccorso, F.; Basko, D. M.; Ferrari, A. C. Graphene Mode-locked Fiber Laser. *ACS Nano* **2010**, *4*, 803-810.

[40] Novoselov, K. S.; Jiang, D.; Schedin, F.; Booth, T. J.; Khotkevich, V. V.; Morozov, S. V.; and Geim,A. K.; Two-dimensional atomic crystals. *P. Natl. Acad. Sci. U.S.A.* **2005**, *102*, 10451-10453.

[41] Karu, A. E.; Beer, M. Pyrolytic Formation of Highly Crystalline Graphite Films. *J. Appl. Phys.* **1966**, *37*, 2179-2181.

[42] Obraztsov, A. N.; Obraztsova, E. A.; Tyurnina, A. V.; and Zolotukhin,A. A. Chemical vapor deposition of thin graphite films of nanometer thickness. *Carbon* **2007**, *45*, 2017-2021.

[43] Kim, K. S.; Zhao,Y.; Jang, H.; Lee, S. Y.; Kim, J. M.; Kim, K. S.; Ahn, J.-H.; Kim, P.; Choi, J.-Y.; Hong, B. H. Large-scale pattern growth of graphene films for stretchable transparent electrodes. *Nature* **2009**, *457*, 706-710.

[44] Reina A.; Jia X.; Ho J.; Nezich D.; Son H.; Bulovic V.; Dresselhaus M.S.; Kong J. Large Area, Few-Layer Graphene Films on Arbitrary Substrates by Chemical Vapor Deposition. *Nano Lett.* **2009** *9*, 30-35.

[45] Li X. S.; Cai W. W.; An J. H.; Kim S.; Nah J.; Yang D. X.; Piner R.; Velamakanni A.; Jung I.; Tutuc E.; Banerjee S. K.; Colombo L.; Ruoff R. S. Large-Area Synthesis of High-Quality and Uniform Graphene Films on Copper Foils, *Science* **2009**, *324*, 1312-1314.

[46] Bae, S.; Kim, H.; Lee, Y.; Xu, X.; Park, J.-S.; Zheng, Y.; Balakrishnan, J.; Lei, T.; Ri Kim, H.; Song, Y. I.; Kim, Y.-J.; Kim, K. S.; Ozyilmaz, B.; Ahn, J.-H.; Hong, B. H.; Iijima, S. Roll-to-roll production of 30-inch graphene films for transparent electrodes. *Nat. Nanotechnol.* **2010**, *5*, 574-578.

[47] Berger, C.; Song, Z.; Li, T.; Li, X.; Ogbazghi, A. Y.; Feng, R.; Dai, Z.; Marchenkov, A. N.; Conrad, E. H.; First, P. N.; de Heer, W. A. Ultrathin Epitaxial Graphite: 2D Electron Gas Properties and a Route toward Graphene-based Nanoelectronics. *J. Phys. Chem. B* **2004**, *108*, 19912-19916.

[48] Acheson, E. G.; Production of artificial crystalline carbonaceous materials; article of carborundum and process of the manufacture thereof carborundum. US patent 615,648 (1896).

[49] Badami, D. V. Graphitization of α-Silicon Carbide, *Nature* **1962**, *193*, 569-570.

[50] Emtsev, K. V.; Bostwick, A.; Horn, K.; Jobst, J.; Kellogg, G. L.; Ley, L.; McChesney, J. L.; Ohta, T.; Reshanov, S. A.; Rohrl, J. *et al.* Towards wafer-size graphene layers by atmospheric pressure graphitization of silicon carbide. *Nat. Mater.* **2009**, *8*,203-207.

[51] Oshima C.; Nagashima A. Ultra-thin epitaxial films of graphite and hexagonal boron nitride on solid surfaces, *J. Phys.: Condens. Matter* **1997**, *9*, 1-20.

[52] Gamo Y.; Nagashima A.; Wakabayashi M.; Terai M.; Oshima C. Atomic structure of mono-layer graphite formed on Ni(111), *Surface Science* **1997**, *374*, 61-64.

[53] Rosei R.; De Crescenzi M.; Sette F.; Quaresima C.; Savoia A.; Perfetti P. Structure of graphitic carbon on Ni(111): A surface extended-energy-loss fine-structure study, *Physical Review B* **1983**, *28*, 1161.

[54] Sutter, P. W.; Flege, J.-I.; Sutter, E. A. Epitaxial graphene on ruthenium. *Nat. Mater.* **2008** *7*, 406-411;

[55] Hernandez, Y.; Nicolosi, V.; Lotya, M.; Blighe, F. M.; Sun, Z.; De, S.; McGovern, I. T.; Holland, B.; Byrne, M.; Gun'Ko, Y. K.; Boland,J. J.; Niraj, P.; Duesberg, G.; Krishnamurthy, S.; Goodhue, R.; Hutchison, J.; Scardaci, V.; Ferrari, A. C.; Coleman, J. N. High-yield production of graphene by liquid-phase exfoliation of graphite. *Nat. Nanotechnol.* **2008**, *3*, 563-568.

[56] Lotya, M.; Hernandez, Y.; King, P. J.; Smith, R. J.; Nicolosi, V.; Karlsson, L. S.; Blighe, F. M.; De, S.; Wang, Z.; McGovern, I. T.; Duesberg G. S.; Coleman, J. N. Liquid Phase Production of Graphene by Exfoliation of Graphite in Surfactant/Water Solutions. *J. Am. Chem. Soc.* **2009**, *131*, 3611-3620.

[57] Valles, C.; Drummond, C.; Saadaoui, H.; Furtado, C. A.; He, M.; Roubeau, O.; Ortolani, L.; Monthioux, M.; Penicaud, A. Solutions of Negatively Charged Graphene Sheets and Ribbons. *J. Am. Chem. Soc.* **2008**, *130*, 15802.

[58] Hasan, T.; Torrisi, F.; Nicolosi, V.; Privitera, G.; Bonaccorso, F.; Ferrari, A.C. Solution-phase exfoliation of graphite for ultrafast photonics. *Phys. Status Solidi B* **2010**, *247*, 2953.

[59] Marago, O. M.; Bonaccorso, F.; Saija, R.; Privitera, G.; Gucciardi, P. G.; Lati, M. A.; Calogero, G.; Jones, P. H.; Borghese, F.; Denti, P.; Nicolosi, V.; Ferrari, A. C. Brownian Motion of Graphene, *ACS Nano* **2010**, *4*, 7515-7523.

[60] Green, A. A.; Hersam, M. C. Solution Phase Production of Graphene with Controlled Thickness via Density Differentiation. *Nano Lett.* **2009**, *9*, 4031-4036.

[61] Li, X. L.; Wang, X. R.; Zhang, L.; Lee, S. W.; Dai,H. J. Chemically derived, ultrasmooth graphene nanoribbon semiconductors. *Science* **2008**, *319*, 1229-1232.

[62] Stankovich, S.; Piner, R. D.; Nguyen, S. T.; Ruoff, R. S.; Synthesis and exfoliation of isocyanate-treated graphene oxide nanoplatelets. *Carbon* **2006**, *44*, 3342-3347.

[63] Hummers, W. S.; Offeman, R. E.; Preparation of Graphitic Oxide. *J. Am. Chem. Soc.* **1958**, *80*, 1339-1339.

[64] Brodie, B. C. Sur le poids atomique du graphite. *Ann. Chim. Phys.* **1860**, *59*, 466-472.

[65] Staudenmaier, L. Verfahren zur Darstellung der Graphitsäure. *Ber. Deut. chem. Ges.* **1898**, *31*, 1481.

[66] Mattevi, C.; Eda, G. ; Agnoli, S.; Miller, S.; Mkhoyan, K. A.; Celik, O.; Mastrogiovanni, D.; Granozzi, G.; Garfunkel, E.; Chhowalla, M. Evolution of Electrical, Chemical, and Structural Properties of Transparent and Conducting Chemically Derived Graphene Thin Films. *Adv. Funct. Mater.* **2009**, *29*, 2577-2583.

[67] Cai, W. W.; Piner, R. D.; Stadermann, F. J.; Park, S.; Shaibat, M. A.; Ishii, Y.; Yang, D. X.; Velamakanni, A.; An, S. J.; Stoller, M.; An, J. H.; Chen, D. M.; Ruoff, R. S. Synthesis and solid-state NMR structural characterization of C-13-labeled graphite oxide. *Science* **2008**, *321*, 1815-1817.

[68] Eda, G.; Chhowalla, M. Chemically Derived Graphene Oxide: Towards Large-Area Thin-Film Electronics and Optoelectronics. *Adv. Mater.* **2010**, *22*, 2392-2415.

32

[69] Paredes, J. I., Villar-Rodil, S., Martinez-Alonso, A. and Tascon, J. M. D., Langmuir, **24**, 10560-10564 (2008).

[70] He, H., Klinowski, J., Forster, M. and Lerf, A., Chem. Phys. Lett., **287**, 53-56 (1998).

[71] Eda, G.; Fanchini,G.; Chhowalla, M. Large-area ultrathin films of reduced graphene oxide as a transparent and flexible electronic material. *Nat. Nanotechnol.* **2008**, *3*, 270-274.

[72] Dua, V.; Surwade, S.; Ammu, S.; Agnihotra, S.; Jain, S.; Roberts, K.; Park, S.; Ruoff, R.; Manohar, S. All-Organic Vapor Sensor Using Inkjet-Printed Reduced Graphene Oxide. *Angew. Chem. Int. Ed.* **2010**, *49*, 2154-2157.

[73] Wang, S.; Ang, P. K.; Wang, Z.; Tang, A. L. L.; Thong J. T. L.; Loh, K. P. High Mobility, Printable, and Solution-Processed Graphene Electronics. *Nano Lett.* **2009**, *10*, 92-98.

[74] Park, B. K.; Kim, D.; Jeong, S.; Moon, J.; Kim, J. S. Direct writing of copper conductive patterns by ink-jet printing, *Thin Solid Films* **2007**, *515*, 7706-7711.

[75] Reis, N.; Derby, B. Ink jet deposition of ceramic suspensions: modelling and experiments of droplet formation, *MRS. Symp. Proc.* **2000**, *624*, 65.

[76] Jang, D.; Kim, D.; Moon, J. Influence of Fluid Physical Properties on Ink-Jet Printability, *Langmuir* **2009**, *25*, 2629-2635.

[77] Fromm, J. E. Numerical-calculation of the fluid-dynamics of drop-on-demand jets, *IBM J. Res. Dev.* **1984**, *28*, 322.

[78] Fluid properties effects on ink-jet device performance, *MicroFab technote* **1999**, online access: http://www.microfab.com/equipment/technotes/technote99-02.pdf.

[79] De Gennes, P. G. Wetting: statics and dynamics. *Rev. Mod. Phys.* **1985**, *57*, 827.

33

[80] Shafrin, E. G.; Zisman, W. A. Constitutive relations in the wetting of low energy surfaces and the theory of the retraction method of preparing monolayers. *J. Phys. Chem.* **1960**, *64*, 519-524.

[81] Israelachvili, J. In *Intermolecular and Surface Forces*; Academic press, New York, **1991**.

[82] Derby, B.; Reis, N. Inkjet printing of highly loaded particulate suspension, *MRS. Bull.* **2003**, *28*, 815.

[83] Park, J. S.; Kim, J. P.; Song, C.; Lee, M. Control of inkjet printed profiles by solvent-vapor annealing. *Displays* **2010**, *31*, 164-167.

[84] Deegan, R. D.; Bakajin, O.; Dupont, T. F.; Huber, G.; Nagel, S. R.; Witten, T. A. Capillary flow as the cause of ring stains from dried liquid drops, *Nature* **1997**, *389*, 827-829.

[85] Osthoff, R. C.; Kantor, S. W. *Organosilazane Compounds* John Wiley & Sons, Inc.; **1997**

[86] Lide, D. R. In *Handbook of Chemistry and physics 86th ed.*; CRC Press Inc.; Boca Raton, FL, **2005**

[87] Mak, K. F.; Sfeir, M. Y.; Wu, Y.; Lui, C. H.; Misewich, J. A.; Heinz, T. F. Measurement of the Optical Conductivity of Graphene. *Phys. Rev. Lett.* **2008**, *101*, 196405.

[88] Kravets, A.; Grigorenko, N.; Nair, R. R.; Blake, P.; Anissimova, S.; Novoselov, K. S.; Geim, A. K. Spectroscopic ellipsometry of graphene and an exciton-shifted van Hove peak in absorption. *Phys. Rev. B* **2010**, *81*, 155413.

[89] Nair, R. R.; Blake, P.; Grigorenko, A. N.; Novoselov, K. S.; Booth, T. J.; Stauber, T.; Peres, N. M. R.; Geim, A. K. Fine Structure Constant Defines Visual Transparency of Graphene. *Science* **2008**, *320*, 1308-1308.

[90] Casiraghi, C.; Hartschuh, A.; Lidorikis, E.; Qian, H.; Harutyunyan, H.; Gokus, T.; Novoselov, K. S.; Ferrari, A. C. Rayleigh Imaging of Graphene and Graphene Layers. *Nano Lett.* **2007**, *7*, 2711-2717.

34

[91] Meyer, J. C.; Geim, A. K.; Katsnelson, M. I.; Novoselov, K. S.; Booth,T. J.; Roth, S.; The structure of suspended graphene sheets. *Nature* **2007**, *446*, 60-63.

[92] Meyer, J. C.; Geim, A. K.; Katsnelson, M. I.; Novoselov, K. S.; Obergfell, D.; Roth, S.; Girit, C.; Zettl, A. On the roughness of single- and bi-layer graphene membranes. *Solid State Comm.* **2007**, *143*, 101-109.

[93] Ferrari, A. C.; Meyer; J. C.; Scardaci, V.; Casiraghi, C.; Lazzeri,M.; Mauri, F.; Piscanec, S.; Jiang, D.; Novoselov, K. S.; Roth, S.; Geim, A. K. Raman spectrum of graphene and graphene layers. *Phys. Rev. Lett.* **2006**, *97*, 4.

[94] Khan, U.; O'Neill, A.; Lotya, M.; De, S.; Coleman, J. N. High-Concentration Solvent Exfoliation of Graphene, *Small* **2010**, *6*, 864-871.

[95] C. M. Hansen, *Hansen Solubility Parameters: A User's Handbook*, CRC Press Inc., **2007** Boca Raton, FL.

[96] Bergin, S. D.; Nicolosi, V.; Streich, P. V.; Giordani, S.; Sun, Z.; Windle, A. H.; Ryan, P.; Niraj, N. P. P.; Wang, Z.-T.; Carpenter, L.; Blau, W. J.; Boland, J. J.; Hamilton, J. P.; and Coleman, J. N. *Adv. Mater.*, **2008**, *20*, 1876.

[97] Lotya, M.; King, P. J.; Khan, U.; De S. and Coleman, J. N. *ACS Nano*, **2010** *4*, 3155-3162.

[98] J. W. Williams; K. E. Van Holde; R. L. Baldwin; H. Fujita, Chem Rev., **1958**, *58*,715-806.

[99] Schuck, P. Biophysical Journal **2000**, *78*,1606Ű1619.

[100] Svedberg, T.; Pedersen, K. O. *The Ultracentrifuge*, Oxford University press, **1940**, London.

[101] Ferrari, A. C.; Robertson, J. Interpretation of Raman spectra of disordered and amorphous carbon. *Phys. Rev. B* **2000**, *61*, 14095-14107.

[102] Tuinstra, F.; Koenig, J. L. Raman spectrum of graphite. *J. Chem. Phys.* **1970**, *53*, 1126-1130.

[103] Piscanec, S.; Lazzeri, M.; Mauri, F.; Ferrari, A. C.; Robertson, J. Kohn anomalies and electron-phonon interactions in graphite, *Phys. Rev. Lett.* **2004**, *93*, 4.

[104] Casiraghi, C.; Hartschuh, A.; Qian, H.; Piscanec, S.; Georgi, C.; Fasoli, A.; Novoselov, K. S.; Basko, D. M.; Ferrari, A. C. *Nano Lett.* **2009**, *9*, 1433-1441.

[105] Ferrari, A. C.; Robertson, *Phys. Rev. B*,**2001**, *64*, 13.

[106] Cancado, L. G.; Jorio, A.; Ferreira, E. H. M.; Stavale, F.; Achete, C. A.; Capaz, R. B.; Moutinho, M. V. O.; Lombardo, A.; Kulmala, T. S.; Ferrari, A. C. *Nano Lett.*, **2011**,*11*, 3190-3196.

[107] Ferrari, A. C.; Rodil, S. E.; Robertson, J. Resonant Raman spectra of amorphous carbon nitrides: the G peak dispersion, *Diamond and Related Materials* **2003** *12*, 905-910.

[108] Ferrari A. C., *Surf. Coat. Tech.*, **2004**,*11*,180-181, 190-206.

[109] Basko, D. M.; Piscanec, S.; Ferrari, A. C. Electron-electron interactions and doping dependence of the two-phonon Raman intensity in graphene, *Physical Review B* **2009**, *80*, 165413.

[110] Das, A.; Pisana, S.; Chakraborty, B.; Piscanec, S.; Saha,S. K.; Waghmare,U. V.; Novoselov, K. S.; Krishnamurthy,H. R.; Geim, A. K.; Ferrari,A. C.; and Sood, A. K. Nat. Nano., 3, 210-215, (2008).

[111] Pisana,S.; Lazzeri, M.; Casiraghi, C.; Novoselov, K. S.; Geim, A. K.; Ferrari, A. C.; and Mauri, F. Nat. Mater., 6, 198-201, (2007).

[112] Kaye, B. H. In *Powder mixing*; Chapman & Hall; London, **1997**).

[113] Kauffman, G. W.; Jurs, P. C. Prediction of Surface Tension, Viscosity, and Thermal Conductivity for Common Organic Solvents Using Quantitative StructureâĽŠProperty Relationships, *Journal of Chemical Information and Computer Sciences* **2001**, *41*, 408-418.

[114] http://www.epson.com/cgi-bin/Store/Landing/InkTechCartridges.jsp access on April 2011.

[115] Young, T. An Essay on the Cohesion of Fluids. *Philos. T. R. Soc. Lon.* **1805**, *95*, 65-87.

[116] Shafrin, E. G.; Zisman, W. A. Critical surface tension for spreading on a liquid substrate. *J. Phys. Chem.* **1967**, *71*, 1309-1316.

[117] Marmur, A. Wetting on Hydrophobic Rough Surfaces: To Be Heterogeneous or Not To Be?. *Langmuir* **2003**, *19*, 8343-8348.

[118] Duineveld, P. C. The stability of ink-jet printed lines of liquid with zero receding contact angle on a homogeneous substrate, *Journal of Fluid Mechanics* **2003**, *477*, 175-200.

[119] Gamerith, S.; Klug, A.; Scheiber, H.; Scherf, U.; Moderegger, E.; List, E. J. W. Direct ink-jet printing of Ag-Cu nanoparticle and Ag-precursor based electrodes for OFET applications. *Adv. Func. Mater.* **2007**, *17*, 3111-3118.

[120] Smits F.M. Measurement of sheet resistivities with the four-probe, Bell Sys. Tech. Jour., 37, 711-718, 1958. , *Bell Sys. Tech. Jour.*

[121] Hu, L.; Hecht, D. S.; Gruner,G. Percolation in Transparent and Conducting Carbon Nanotube Networks, *Nano Lett.* **2004**, *4*, 2513.

[122] Geng, H. Z.; Kim, K. K.; So, K. P.; Lee, Y. S.; Chang, Y.; Lee, Y. H. *J. Am. Chem. Soc.* **2007**, *129*, 7758.

[123] De, S.; King, P. J.; Lyons, P. E.; Khan, U.; Coleman, J. N. Size Effects and the Problem with Percolation in Nanostructured Transparent Conductors, *ACS Nano* **2010** *4*, 7064-7072.

[124] De, S.; King, P. J.; Lotya, M.; O'Neill, A.; Doherty, E. M.; Hernandez, Y.; Duesberg, G. S.; Coleman, J. N. Flexible, Transparent, Conducting Films of Randomly Stacked Graphene from Surfactant-Stabilized, Oxide-Free Graphene Dispersions, **2009** *Small 6*, 458-464.

[125] Kirkpatrick, S. Percolation and Conduction. *Rev. Mod. Phys.* **1973**, *45*, 574.

[126] Stauffer, D.; Aharony, A. In *Introduction to percolation theory*, Taylor&Francis: London, **1985**.

[127] Kogut, P. M.; Straley, J. P. Distribution-induced non-universality of the percolation conductivity exponents, *Journal of Physics C: Solid State Physics* **1979**, *12*, 2151.

[128] Johner, N.; Grimaldi, C.; Balberg, I.; Ryser, P. Transport exponent in a three-dimensional continuum tunneling-percolation model, *Physical Review B* **2008**, *77*, 174204.

[129] Doherty, E. M.; De, S.; Lyons, P. E.; Shmeliov, A.; Nirmalraj, P. N.; Scardaci, V.; Joimel, J.; Blau, W. J.; Boland, J. J.; Coleman, J. N. The spatial uniformity and electromechanical stability of transparent, conductive films of single walled nanotubes, *Carbon* **2009**, *47*, 2466-2473.

[130] Kuzmenko, A. B.; van Heumen, E.; Carbone, F.; van der Marel, D. Universal Optical Conductance of Graphite, *Physical Review Letters* **2008**, *100*, 117401.

[131] Ong, B. S.; Wu, Y.; Liu, P.; Gardner, S.; High-Performance Semiconducting Polythiophenes for Organic Thin-Film Transistors. *J. Am. Chem. Soc.* **2004**, *126*, 3378-3379.

[132] Arias, A. C.; Ready, S. E.; Lujan, R.; Wong, W. S.; Paul, K. E.; Salleo, A.; Chabinyc, M. L.; Apte, R.; Street, R. A.; Wu, Y.; Liu, P.; Ong, B. All jet-printed polymer thin-film transistor active-matrix backplanes. *Appl. Phys. Lett.* **2004**, *85*, 3304-3306.

[133] Wu, Y.; Liu, P.; Ong, B. S.; Srikumar, T.; Zhao, N.; Botton, G.; Zhu, S. Controlled orientation of liquid-crystalline polythiophene semiconductors for high-performance organic thin-film transistors. *Appl. Phys. Lett.* **2005**, *86*, 142102.

[134] Kaneto, K.; Yano, M.; Shibao, M.; Morita, T.; Takashima, W. Ambipolar Field-Effect Transistors Based on Poly(3-hexylthiophene)/Fullerene Derivative Bilayer Films, *J. J. App. Phys.* **2007**, *46*, 1736 - 1738.

38

[135] Morita, T.; Singh, V.; Oku, S.; Nagamatsu, S.; Takashima, W.; Hayase, S.; Kaneto, K. Ambipolar Transport in Bilayer Organic Field-Effect Transistor Based on Poly(3-hexylthiophene) and Fullerene Derivatives, *J. J. App. Phys.* **2010**, *49*, 04161 - 04166.

[136] Oh, J. H.; Lee, H. W.; Mannsfeld, S.; Stoltenberg, R. M.; Jung, E.; Jin, Y. W.; Kim, J. M.; Yoo, J.-B.; Bao, Z. Solution-processed, high-performance n-channel organic microwire transistors. *P. Natl. Acad. Sci. U.S.A.* **2009**, *106*, 6065-6070.

[137] Sirringhaus, H.; Tessler, N.; Friend, R. H. Integrated Optoelectronic Devices Based on Conjugated Polymers, *Science* **1998**, *280*, 1741-1744.

[138] Song, Y.J.;, Lee, J. U.; Jo, W.H. Multi-walled carbon nanotubes covalently attached with poly(3-hexylthiophene) for enhancement of field-effect mobility of poly(3-hexylthiophene)/multi-walled carbon nanotube composites, *Carbon* **2010** *48*, 389-395.

[139] Whiting, G. L. and Arias, A. C. Chemically modified ink-jet printed silver electrodes for organic field-effect transistors, *Appl. Phys. Lett.* **2009**, *95*, 253302-3.

[140] Klauk, H. In *Organic Electronics*, Wiley-VCH: Weinheim, **2006**; Chapter 4.

[141] Chason, M.; Brazis, P. W., Zhang, J.; Kalyanasundaram, K.; Gamota, D. R. Printed Organic Semiconducting Devices, *Proc. IEEE* **2005**, *93*, 1348.

[142] Kawase, T.; Moriya, S.; Newsome, C. J.; Shimoda, T. Inkjet Printing of Polymeric Field-Effect Transistors and Its Applications. *J. J. App. Phys.* **2005**, *44*, 3649-3658.

[143] Parmer, J. E.; Mayer, A. C.; Hardin, B. E.; Scully, S. R.; McGehee, M. D.; Heeney, M.; McCulloch, I. Organic bulk heterojunction solar cells using poly(2,5-bis(3-tetradecyllthiophen-2-yl)thieno[3,2,-b]thiophene). *Appl. Phys. Lett.* **2008**, *92*, 113309-3.

[144] Padday, J. F. The Profiles of Axially Symmetric Menisci. *Phyl. Trans. R. Soc. Lond. A* **1971**, *269*, 265.